MILCOM 2024 - 2024 IEEE Military Communications Conference (MILCOM) | 979-8-3503-7423-0/24/$31.00 ©2024 IEEE | DOI: 10.1109/MILCOM61039.2024.10774026

Location Verification in Next-Generation Non-Terrestrial Networks

Nathan Schatz*† Seungnyun Kim* Girim Kwon* Bernardo Camajori Tedeschini* Michael Ricard† Tyler Klein† Vijitha Weerackody‡ Andrea Conti§ and Moe Z. Win††

*Wireless Information and Network Sciences Laboratory, Massachusetts Institute of Technology, Cambridge, MA, USA
†Charles Stark Draper Laboratory, Inc., Cambridge, MA, USA
‡Applied Physics Laboratory, Johns Hopkins University, Laurel, MD, USA
§Department of Engineering and CNIT, University of Ferrara, Ferrara, Italy
††Laboratory for Information and Decision Systems, Massachusetts Institute of Technology, Cambridge, MA, USA

***Abstract*—Reliable location awareness is essential for the development of new services and applications in non-terrestrial networks (NTNs). The ability of malicious users to report false location information poses a significant threat to the performance of NTNs. This threat introduces the need for a flexible and robust location verification system (LVS) that can reliably detect malicious users. This paper proposes a single-satellite LVS based on round-trip time and angle-of-arrival measurements. We characterize several sources of uncertainty unique to NTNs and examine their combined effect on positioning error. Using this model, we approximate a likelihood function for the unknown user position and propose a likelihood ratio decision rule for location verification. Results display receiver operating characteristic (ROC) curves to evaluate the LVS performance when a malicious user is located at various distances from its reported location. When compared with two other baseline LVSs, the proposed system is shown to significantly improve area under the ROC curve performance.**

***Index Terms*—Non-terrestrial networks, network verified location, round-trip time, angle-of-arrival, location verification system.**

I. Introduction

Location awareness in next generation (xG) networks is critical for optimized network performance, resource management, and many other applications [1]–[4]. In non-terrestrial networks (NTNs), accurate position data can enhance command-and-control capability in remote areas, enable efficient management of satellite handover, and ensure seamless integration with terrestrial infrastructure [5]–[7]. As cellular systems push towards ubiquitous global connectivity enabled by NTNs, the need for awareness of user equipment (UE) location information continues to grow [8]–[11].

The coverage areas of low earth orbit (LEO) satellites in NTNs can extend for thousands of kilometers, thus limiting the value of cell-ID location information immediately available to the network [8], [12]. Malicious users can potentially tamper with NTNs by spoofing their reported location information [9]. This can hinder law enforcement or network governance activities, introduce ambiguity regarding appropriate core network selection, and degrade network performance by interfering with resource allocation within the LEO network itself [8], [13], [14]. In the event that the coverage area of a single satellite reaches across national boundaries, an attacker can exploit this ambiguity by connecting to an inappropriate public land mobile network in order to circumvent regulation or evade law enforcement [8], [15]. These possibilities introduce the need for a reliable NTN location verification system (LVS) that can detect UEs reporting spoofed location information to the network. According to the 3rd Generation Partnership Project (3GPP), a satellite network must independently verify UE location to within 5-10 km [9].

Various methods have been proposed which depend on radio access technology to verify UE location in NTNs. In [16], the authors propose a time difference-of-arrival positioning method involving multiple satellites. This method exploits spatial diversity in satellite mega-constellations to estimate UE location, but requires all nodes to communicate with a central processing center, thus potentially suffering from geometric dilution of precision (GDOP) [16], [17]. Methods based solely on round-trip time (RTT) also require multiple measurements with spatial diversity for a position estimate and thus can also be affected by GDOP. In [18], the authors present a method for localization of remote nodes based on a fusion of RTT and Doppler measurements. However, Doppler-based techniques are limited in their spoofing resilience because a malicious UE has direct control over its transmitting frequency [19].

We propose a novel UE LVS based on angle-of-arrival (AOA) and RTT measurements from a single satellite. This method avoids the detrimental effects of GDOP by reducing the total number of measurements required. Additionally, the AOA measurement limits the ability of a malicious UE to tamper with location estimation inputs. First, we enumerate and investigate the effects of realistic sources of uncertainty on the model, then we approximate the noise probability distribution function (PDF) using a Gaussian mixture model (GMM) to formulate a likelihood ratio test. Finally, we compare the proposed LVS against two baseline decision rules and evaluate its performance.

Notations: Random variables are displayed in sans serif, upright fonts; their realizations in serif, italic fonts. Vectors

The fundamental research described in this paper was supported, in part, by the Draper Scholars Program, by the Office of Naval Research under Grant N62909-22-1-2009, by the National Science Foundation under Grant CNS-2148251, and by federal agency and industry partners in the RINGS program.
Corresponding author: Moe Z. Win (e-mail: moewin@mit.edu).

and matrices are denoted by bold lowercase and uppercase letters, respectively. For example, a random variable and its realization are denoted by x and x; a random vector and its realization are denoted by $\mathbf{x}$ and $\boldsymbol{x}$; a matrix is denoted by $\boldsymbol{X}$, respectively. Sets are denoted by calligraphic font, and a set complements are denoted by a bar. For example, a set and its complement are denoted by $\mathcal{X}$ and $\overline{\mathcal{X}}$. The determinant, Euclidean norm, and transpose operations are denoted by $|\cdot|$, $\|\cdot\|$, and $[\cdot]^{\mathrm{T}}$, respectively.

II. System Model

In this section we define a noiseless system model relating geometry, verified acceptance regions, and noiseless measurements. Noise and uncertainty will be applied to the model in Section III.

A. Geometric Model for LEO Network

Consider a UE on the surface of the earth located at the position $\boldsymbol{u} = [\,u_{\mathrm{x}}\ u_{\mathrm{y}}\ u_{\mathrm{z}}\,]^{\mathrm{T}}$ in the Earth-Centered-Earth-Fixed (ECEF) coordinate reference frame. This UE is in the field of view (FoV) of a single LEO satellite orbiting above and connected to it. The LEO satellite is able to obtain RTT and two-dimensional AOA measurements from the UE. In addition, consider three ECEF points on the LEO orbit: the point $\boldsymbol{p}_{\mathrm{t}} = [\,p_{\mathrm{t,x}}\ p_{\mathrm{t,y}}\ p_{\mathrm{t,z}}\,]^{\mathrm{T}}$ where the satellite transmits its downlink (DL) packet for RTT measurement, the point $\boldsymbol{p}_{\mathrm{r}} = [\,p_{\mathrm{r,x}}\ p_{\mathrm{r,y}}\ p_{\mathrm{r,z}}\,]^{\mathrm{T}}$ where the satellite receives the uplink (UL) packet responding to the DL packet, and the point $\boldsymbol{p}_{\mathrm{a}} = [\,p_{\mathrm{a,x}}\ p_{\mathrm{a,y}}\ p_{\mathrm{a,z}}\,]^{\mathrm{T}}$ where the satellite performs AOA estimation on an UL signal from the UE. The instantaneous satellite velocities at these three points are denoted by $\boldsymbol{v}_{\mathrm{t}} = [\,v_{\mathrm{t,x}}\ v_{\mathrm{t,y}}\ v_{\mathrm{t,z}}\,]^{\mathrm{T}}$, $\boldsymbol{v}_{\mathrm{r}} = [\,v_{\mathrm{r,x}}\ v_{\mathrm{r,y}}\ v_{\mathrm{r,z}}\,]^{\mathrm{T}}$, and $\boldsymbol{v}_{\mathrm{a}} = [\,v_{\mathrm{a,x}}\ v_{\mathrm{a,y}}\ v_{\mathrm{a,z}}\,]^{\mathrm{T}}$, respectively. Fig. 1 illustrates this geometric reference system.

B. UE Acceptance Region

Upon request from the satellite, the UE reports its own position estimate $\boldsymbol{u}_{\mathrm{c}} = [\,u_{\mathrm{c,x}}\ u_{\mathrm{c,y}}\ u_{\mathrm{c,z}}\,]^{\mathrm{T}}$ to the satellite [8], [20]. A *compliant user* reports its true position estimate, while a *malicious user* reports a spoofed position. This reported position $\boldsymbol{u}_{\mathrm{c}}$ defines the acceptance region $\mathcal{A}$, i.e., the region of points on Earth's surface near $\boldsymbol{u}_{\mathrm{c}}$ that are considered acceptable locations for the true position $\boldsymbol{u}$ of a compliant user by 3GPP or other authorities. The objective of the LVS is to verify the null hypothesis H_0: the event that a UE's true position $\boldsymbol{u}$ lies within the acceptance region corresponding to its reported position $\boldsymbol{u}_{\mathrm{c}}$. The alternative hypothesis H_1 is the event that the UE's true position lies outside the acceptance region due to a malicious UE report. These hypotheses are summarized as

$$H_0 : \boldsymbol{u} \in \mathcal{A} \tag{1}$$
$$H_1 : \boldsymbol{u} \in \overline{\mathcal{A}}\,. \tag{2}$$

According to 3GPP [9], $\mathcal{A}$ is described as a region containing all points within 5-10 km from $\boldsymbol{u}_{\mathrm{c}}$. In practice, however, both $\mathcal{A}$ and $\overline{\mathcal{A}}$ have arbitrary geometry based on national boundaries or immediate needs of the system. For the purposes of this work, let $\mathcal{A}$ be the set of points on Earth's surface within 5 km from $\boldsymbol{u}_{\mathrm{c}}$.

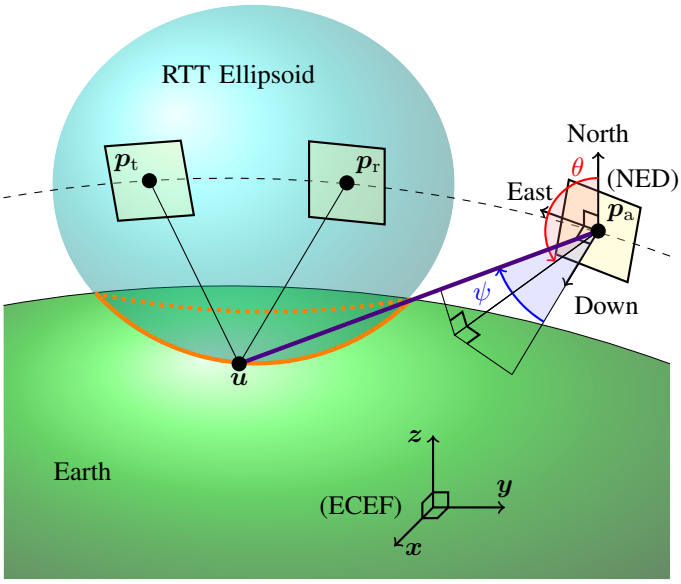

Fig. 1: Geometric reference system. The yellow polygons represent the nadir-pointing satellite antenna array at different positions in orbit. In the local coordinate reference frame of the satellite, θ and ψ represent the azimuth and off-nadir angles, respectively. Note that this figure represents a compliant user, reporting its true position estimate.

C. Noiseless Measurement Model

In the absence of noise or uncertainty, the true UE position $\boldsymbol{u}$ can be uniquely determined from the intersection of the RTT oblate ellipsoid and AOA line, as shown in Figure 1. The surface of the RTT ellipsoid represents all points whose pseudoranges from the foci $\boldsymbol{p}_{\mathrm{t}}$ and $\boldsymbol{p}_{\mathrm{r}}$ sum to a constant τ, as detailed below in (3a). The AOA line in 3D space represents all points colinear with $\boldsymbol{u}$ and $\boldsymbol{p}_{\mathrm{a}}$. We consider the North-East-Down (NED) coordinate reference frame with respect to the satellite, with the origin defined as the AOA measurement point $\boldsymbol{p}_{\mathrm{a}}$. The positive "North" axis points towards geodetic north along the meridian of the satellite's longitude λ, the positive "East" axis points towards geodetic east along the the parallel of the satellite's latitude ϕ, and the positive "Down" axis points downward along the ellipsoid normal [21]. In the NED coordinate reference frame of the satellite, the incident angles of the AOA line with the antenna array plane are denoted as the azimuth angle θ and off-nadir angle ψ, as shown in Fig. 1. Geometrically, the ellipsoid and line can be defined by $\tau(\boldsymbol{u}, \boldsymbol{p}_{\mathrm{t}}, \boldsymbol{p}_{\mathrm{r}})$, $\theta(\boldsymbol{u}, \boldsymbol{p}_{\mathrm{a}})$, and $\psi(\boldsymbol{u}, \boldsymbol{p}_{\mathrm{a}})$, which satisfy the following relations:

$$\tau(\boldsymbol{u}, \boldsymbol{p}_{\mathrm{t}}, \boldsymbol{p}_{\mathrm{r}}) = \frac{\|\boldsymbol{p}_{\mathrm{t}} - \boldsymbol{u}\| + \|\boldsymbol{p}_{\mathrm{r}} - \boldsymbol{u}\|}{c} \tag{3a}$$
$$\theta(\boldsymbol{u}, \boldsymbol{p}_{\mathrm{a}}) = \arctan\left(\frac{\boldsymbol{u}_{\mathrm{NED}}[2]}{\boldsymbol{u}_{\mathrm{NED}}[1]}\right) \tag{3b}$$
$$\psi(\boldsymbol{u}, \boldsymbol{p}_{\mathrm{a}}) = \arccos\left(\frac{\boldsymbol{u}_{\mathrm{NED}}[3]}{\|\boldsymbol{u} - \boldsymbol{p}_{\mathrm{a}}\|}\right) \tag{3c}$$

where c represents the speed of light, and $\boldsymbol{u}_{\text{NED}} = [\, u_{\text{N}} \;\; u_{\text{E}} \;\; u_{\text{D}} \,]^{\text{T}}$ is a transformation of $\boldsymbol{u}$ into the satellite's NED coordinate reference frame according to the following:

$$\boldsymbol{u}_{\text{NED}} = \boldsymbol{R}(\boldsymbol{u} - \boldsymbol{p}_{\text{a}}) \tag{4}$$

where $\boldsymbol{R}$ is the ECEF-to-NED coordinate transformation matrix given by:

$$\boldsymbol{R} = \begin{bmatrix} -\sin\phi\cos\lambda & -\sin\phi\sin\lambda & \cos\phi \\ -\sin\lambda & \cos\lambda & 0 \\ -\cos\phi\cos\lambda & -\cos\phi\sin\lambda & -\sin\phi \end{bmatrix}. \tag{5}$$

In (5), ϕ and λ representing the geodetic latitude and longitude, respectively, of the satellite at point $\boldsymbol{p}_{\text{a}}$ using the World Geodetic System 1984 (WGS84) global datum. These can be approximated to an arbitrary degree of precision using efficient and well-documented numerical methods [22].

III. RTT/AOA-Based Location Verification System

In reality, there are several independent sources of uncertainty that corrupt the measurement model, which can be described as measurement noise. This section models this noise and applies it to the noiseless model defined above.

A. Noise Modeling

Let $\mathbf{m}$ be a zero-mean, uncorrelated, multivariate Gaussian random vector in which each component represents an independent source of additive error within the measurement model. Satellite position uncertainty is one source of error which affects all satellite measurements. Let the uncertain satellite position estimates be represented by

$$\hat{\mathbf{p}}_{\text{t}} = \boldsymbol{p}_{\text{t}} + \mathbf{m}_{\text{t}} \tag{6a}$$

$$\hat{\mathbf{p}}_{\text{r}} = \boldsymbol{p}_{\text{r}} + \mathbf{m}_{\text{r}} \tag{6b}$$

$$\hat{\mathbf{p}}_{\text{a}} = \boldsymbol{p}_{\text{a}} + \mathbf{m}_{\text{a}} \tag{6c}$$

where $\mathbf{m}_{\text{t}}$, $\mathbf{m}_{\text{r}}$, and $\mathbf{m}_{\text{a}}$ are computed as:

$$\mathbf{m}_{\text{x}} = \mathsf{m}_{\text{rad}} \frac{-\boldsymbol{p}_{\text{x}}}{\|\boldsymbol{p}_{\text{x}}\|} + \mathsf{m}_{\text{along}} \left(\frac{-\boldsymbol{p}_{\text{x}}}{\|\boldsymbol{p}_{\text{x}}\|} \times \left(\frac{-\boldsymbol{p}_{\text{x}}}{\|\boldsymbol{p}_{\text{x}}\|} \times \frac{\boldsymbol{v}_{\text{x}}}{\|\boldsymbol{v}_{\text{x}}\|} \right) \right) + \mathsf{m}_{\text{cross}} \left(\frac{-\boldsymbol{p}_{\text{x}}}{\|\boldsymbol{p}_{\text{x}}\|} \times \frac{\boldsymbol{v}_{\text{x}}}{\|\boldsymbol{v}_{\text{x}}\|} \right) \tag{7}$$

with the placeholder subscript $\text{x} \in \{\text{t}, \text{r}, \text{a}\}$ as appropriate, and $\times$ denoting the vector cross product. The random variables m_{rad}, $\mathsf{m}_{\text{along}}$, and $\mathsf{m}_{\text{cross}}$ represent the satellite position error in the radial, along-track, and cross-track directions, respectively. Equation (7) ensures that m_{rad}, $\mathsf{m}_{\text{along}}$, and $\mathsf{m}_{\text{cross}}$ are applied independently by using the satellite's local and strictly orthogonal Radial-Transverse-Normal (RTN) reference frame [23].

The uncertain satellite position estimates can be added to the measurement model along with the remaining additive error sources considered in this paper. The resulting noisy measurement vector $\hat{\boldsymbol{\eta}} = [\, \hat{\tau} \;\; \hat{\theta} \;\; \hat{\psi} \,]^{\text{T}}$ can be described as

$$\hat{\tau} = \tau(\boldsymbol{u},\, \hat{\mathbf{p}}_{\text{t}},\, \hat{\mathbf{p}}_{\text{r}}) + \mathsf{m}_{\text{RTT}} \tag{8a}$$

$$\hat{\theta} = \theta(\boldsymbol{u},\, \hat{\mathbf{p}}_{\text{a}}) + \mathsf{m}_{\text{az}} + \mathsf{m}_{\text{AOA,az}} \tag{8b}$$

$$\hat{\psi} = \psi(\boldsymbol{u},\, \hat{\mathbf{p}}_{\text{a}}) + \mathsf{m}_{\text{on}} + \mathsf{m}_{\text{AOA,on}} \tag{8c}$$

Algorithm 1 Additive noise isolation

1: Generate valid $\boldsymbol{p}_{\text{t}}$, $\boldsymbol{p}_{\text{r}}$, $\boldsymbol{p}_{\text{a}}$, and $\boldsymbol{u}$, (considering realistic orbits, timing, and FoV)
2: Calculate $\boldsymbol{\eta} = [\, \tau(\boldsymbol{u}, \boldsymbol{p}_{\text{t}}, \boldsymbol{p}_{\text{r}}) \;\; \theta(\boldsymbol{u}, \boldsymbol{p}_{\text{a}}) \;\; \psi(\boldsymbol{u}, \boldsymbol{p}_{\text{a}}) \,]^{\text{T}}$
3: **for** $i = 1$ to 10^6 **do**
4: Generate $\boldsymbol{m}$, a realization of the random vector $\mathbf{m}$
5: Using $\boldsymbol{m}$, calculate $\hat{\boldsymbol{\eta}} = [\, \hat{\tau} \;\; \hat{\theta} \;\; \hat{\psi} \,]^{\text{T}}$
6: $\boldsymbol{n}_i \leftarrow \hat{\boldsymbol{\eta}} - \boldsymbol{\eta}$
7: **end for**
8: Repeat for various choices of $\boldsymbol{p}_{\text{t}}$, $\boldsymbol{p}_{\text{r}}$, $\boldsymbol{p}_{\text{a}}$, and $\boldsymbol{u}$ in order to verify assumption of noise independence from parameter values

where m_{RTT} represents the round-trip time error, m_{az} and m_{on} represent the satellite attitude error in the azimuth and off-nadir orientations, respectively, $\mathsf{m}_{\text{AOA,az}}$ and $\mathsf{m}_{\text{AOA,on}}$ represent the azimuth and off-nadir AOA estimation errors, respectively.

B. Gaussian Mixture Model Approximation

As shown in (6a)–(6c) and (8a)–(8c), some of the random components of $\mathbf{m}$ are applied to parameters through the functions $\tau(\cdot)$, $\theta(\cdot)$, and $\psi(\cdot)$. In order to determine the likelihood of a given measurement based on UE position, we start by approximating the measurement noise distribution as purely additive. This allows us to isolate the desirable effect of the UE position from the undesirable measurement noise $\mathbf{n} = [\, \mathsf{n}_{\tau} \;\; \mathsf{n}_{\theta} \;\; \mathsf{n}_{\psi} \,]^{\text{T}}$:

$$\hat{\tau} \approx \tau(\boldsymbol{u}, \boldsymbol{p}_{\text{t}}, \boldsymbol{p}_{\text{r}}) + \mathsf{n}_{\tau} \tag{9a}$$

$$\hat{\theta} \approx \theta(\boldsymbol{u}, \boldsymbol{p}_{\text{a}}) + \mathsf{n}_{\theta} \tag{9b}$$

$$\hat{\psi} \approx \psi(\boldsymbol{u}, \boldsymbol{p}_{\text{a}}) + \mathsf{n}_{\psi} \tag{9c}$$

or equivalently:

$$\hat{\boldsymbol{\eta}} \approx \boldsymbol{\eta}(\boldsymbol{u}, \boldsymbol{p}_{\text{t}}, \boldsymbol{p}_{\text{r}}, \boldsymbol{p}_{\text{a}}) + \mathbf{n} \tag{10}$$

where $\boldsymbol{\eta}(\cdot) = [\, \tau(\cdot) \;\; \theta(\cdot) \;\; \psi(\cdot) \,]^{\text{T}}$ is a deterministic vector of the geometric functions of interest as described in Section II.

In order to determine the PDF of $\mathbf{n}$, we perform a Monte Carlo simulation following Algorithm 1 by approximating the noise as purely additive. Then, we fit a multivariate GMM to the collected data as an approximation of $\mathbf{n}$. Since each of our input noise components are Gaussian, and a learned mixture of Gaussians can reliably approximate many arbitrary PDFs [24], we can be reasonably confident that a GMM will be an appropriate model for approximating $\mathbf{n}$.

We use the expectation maximization (EM) algorithm to learn the probability distribution of $\mathbf{n}$ as a multivariate GMM, where K represents the number of Gaussian components [25]. We choose K such that the resulting model satisfies the minimum Akaike information criterion (AIC). The GMM can be represented as:

$$f_{\mathbf{n}}(\boldsymbol{n}) = \sum_{k=1}^{K} \pi_k \varphi(\boldsymbol{n}; \boldsymbol{\mu}_k, \boldsymbol{\Sigma}_k) \tag{11}$$

Algorithm 2 Proposed LVS performance evaluation

Generate valid $\boldsymbol{p}_\mathrm{t}$, $\boldsymbol{p}_\mathrm{r}$, $\boldsymbol{p}_\mathrm{a}$, and $\boldsymbol{u}$, (considering realistic orbits, timing, and FoV)
Obtain a noisy measurement vector $\hat{\boldsymbol{\eta}}$ using Equations (8a)–(8c)
Choose χ based on desired ROC operating point
$\boldsymbol{u}_\mathrm{c} \leftarrow \boldsymbol{u}$ ▷ Compliant UE
Partition FoV into $\mathcal{A}$ and $\overline{\mathcal{A}}$
Compute $R(\hat{\boldsymbol{\eta}}; \mathcal{A})$
if $R(\hat{\boldsymbol{\eta}}; \mathcal{A}) < \chi$ **then** ▷ Decide H_1
    Type I error: false alarm
else
    Verification of compliant UE
end if
$\boldsymbol{u}_\mathrm{c} \leftarrow$ random point $\in \overline{\mathcal{A}}$ ▷ Malicious UE
Re-partition FoV into $\mathcal{A}$ and $\overline{\mathcal{A}}$
Compute $R(\hat{\boldsymbol{\eta}}; \mathcal{A})$
if $R(\hat{\boldsymbol{\eta}}; \mathcal{A}) > \chi$ **then** ▷ Decide H_0
    Type II error: missed detection
else
    Detection of malicious UE
end if

where $\sum_k \pi_k = 1$ and $\varphi(\boldsymbol{n}; \boldsymbol{\mu}_k, \boldsymbol{\Sigma}_k)$ represents the k-th multivariate Gaussian PDF as described below:

$$\varphi(\boldsymbol{n}; \boldsymbol{\mu}_k, \boldsymbol{\Sigma}_k) = \frac{1}{(2\pi)^{3/2}|\boldsymbol{\Sigma}_k|} \exp\left(-\frac{1}{2}(\boldsymbol{n}-\boldsymbol{\mu}_k)^\mathrm{T} \boldsymbol{\Sigma}_k^{-1} (\boldsymbol{n}-\boldsymbol{\mu}_k)\right) \quad (12)$$

where $\boldsymbol{\mu}_k$ and $\boldsymbol{\Sigma}_k$ represent the mean vector and covariance matrix, respectively, for the k-th Gaussian component.

C. Likelihood Ratio Testing

This formulation allows us to define the measurement likelihood function, or the probability of observing a measurement vector $\boldsymbol{\eta}$ given the true 3D user position vector $\boldsymbol{u}$ using (10). Assuming a non-Bayesian environment without *a priori* information about the probability of encountering a malicious UE, an approximation of the likelihood function of a candidate UE position $\boldsymbol{u}'$ can be computed as

$$\mathscr{L}(\boldsymbol{u}'; \hat{\boldsymbol{\eta}}) = f_{\hat{\boldsymbol{\eta}}}(\hat{\boldsymbol{\eta}}; \boldsymbol{u}') \approx f_{\mathbf{n}}(\hat{\boldsymbol{\eta}} - \boldsymbol{\eta}(\boldsymbol{u}')) = \sum_{k=1}^{K} \pi_k \varphi(\hat{\boldsymbol{\eta}} - \boldsymbol{\eta}(\boldsymbol{u}'); \boldsymbol{\mu}_k, \boldsymbol{\Sigma}_k)\,. \quad (13)$$

According to the Neyman-Pearson lemma, the optimal way to infer the correct set of hypothesized parameters is by comparing their resulting ratios of the likelihood functions of the observed measurements against a scalar threshold value χ [26]. This threshold value χ can be chosen for a desired false alarm rate, which represents a point on the receiver operating characteristic (ROC) curve. To verify the position of the user within a given acceptance region $\mathcal{A}$, we compare the ratio of the likelihood function integrated over the surface areas of interest. The threshold serves as a discriminator between the null hypothesis of a typical honest UE (H_0) and the alternate hypothesis of a malicious UE which is spoofing its location (H_1).

$$R(\hat{\boldsymbol{\eta}}; \mathcal{A}) = \frac{\iint_{\mathcal{A}} \mathscr{L}(\boldsymbol{u}'; \hat{\boldsymbol{\eta}}) d\boldsymbol{u}'}{\iint_{\overline{\mathcal{A}}} \mathscr{L}(\boldsymbol{u}'; \hat{\boldsymbol{\eta}}) d\boldsymbol{u}'} \underset{H_1}{\overset{H_0}{\gtrless}} \chi\,. \quad (14)$$

We compare this decision rule against two baseline decision rules: the reported likelihood threshold and the generalized likelihood ratio test (GLRT). The reported likelihood threshold method, as described by (15), directly compares the likelihood of the reported position $\boldsymbol{u}_\mathrm{c}$ with a threshold value. The GLRT, as described by (16), is an extension of the simple point likelihood ratio to the maximum likelihood within a given region [27].

$$B_1(\hat{\boldsymbol{\eta}}; \boldsymbol{u}_\mathrm{c}) = \mathscr{L}(\boldsymbol{u}_\mathrm{c}; \hat{\boldsymbol{\eta}}) \underset{H_1}{\overset{H_0}{\gtrless}} \chi \quad (15)$$

$$B_2(\hat{\boldsymbol{\eta}}; \mathcal{A}) = \frac{\max_{\boldsymbol{u}' \in \mathcal{A}} \mathscr{L}(\boldsymbol{u}'; \hat{\boldsymbol{\eta}})}{\max_{\boldsymbol{u}' \in \overline{\mathcal{A}}} \mathscr{L}(\boldsymbol{u}'; \hat{\boldsymbol{\eta}})} \underset{H_1}{\overset{H_0}{\gtrless}} \chi\,. \quad (16)$$

The decision rules described by (14)-(16) are compared based on ROC curves for different values of χ. The steps for evaluating the performance of these decision systems are summarized in Algorithm 2.

TABLE I
INPUT NOISE VECTOR COMPONENTS

Name	Std. Dev.	Description
m_rad	1 [m]	Satellite radial position error [29]
$\mathsf{m}_\mathrm{along}$	3 [m]	Satellite along-track position error [29]
$\mathsf{m}_\mathrm{cross}$	2 [m]	Satellite cross-track position error [29]
m_az	0.2 [deg]	Satellite azimuth attitude error [30]
m_on	0.2 [deg]	Satellite off-nadir attitude error [30]
m_RTT	1 [ms]	Round-trip time error [31], [32]
$\mathsf{m}_\mathrm{AOA,az}$	0.5 [deg]	Azimuth AOA measurement error [33]
$\mathsf{m}_\mathrm{AOA,on}$	0.5 [deg]	Off-nadir AOA measurement error [33]

IV. NUMERICAL RESULTS

For the analysis and simulation in this paper, we consider the BLUEWALKER 3 satellite with an approximate orbital height of 500 km and a FoV of (7×10^6) km^2 [28]. We use the WGS84 ellipsoidal model of earth. Orbits are referenced from publicly-available Two-Line-Element (TLE) files and simulated in MATLAB® using the SGP4 orbit propagator.

A. Noise Modeling

The random scalar components of the input noise vector $\mathbf{m}$ and their standard deviations are summarized in Table I. Performing the Monte Carlo simulation as detailed in Algorithm 1 and passing the resulting data points of $\boldsymbol{n}$ to the EM algorithm consistently resulted in a minimum AIC of $K = 1$.

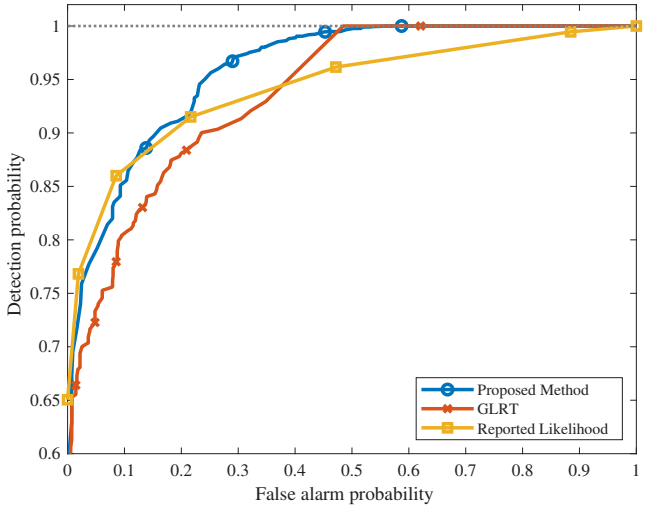

Fig. 2: Overall receiver operating characteristic curve with varying χ using 5-25 km spoofing distances.

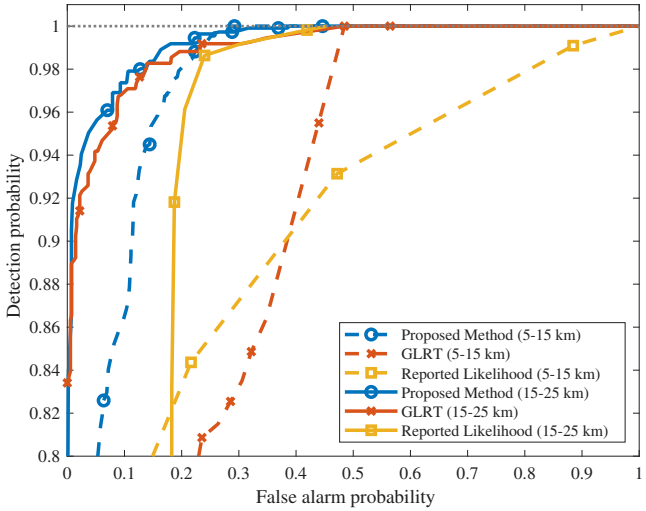

Fig. 3: Comparison of ROC curves at different spoofing distances. Dashed lines represent close spoofing distances (5-15 km) and solid lines represent far spoofing distances (15-25 km).

This implies that $\boldsymbol{n}$ can be most accurately approximated as a Gaussian in three dimensions as shown below

$$f_{\mathbf{n}}(\boldsymbol{n}) = \varphi(\boldsymbol{n}; \boldsymbol{\mu}, \boldsymbol{\Sigma}) \,. \tag{17}$$

This is due to the fact that $\|\mathbf{m}_{\mathrm{t}}\| \ll \|\boldsymbol{p}_{\mathrm{t}}\|$, $\|\mathbf{m}_{\mathrm{r}}\| \ll \|\boldsymbol{p}_{\mathrm{r}}\|$, and $\|\mathbf{m}_{\mathrm{a}}\| \ll \|\boldsymbol{p}_{\mathrm{a}}\|$, therefore it is appropriate to model their effects on $\tau(\cdot)$, $\theta(\cdot)$, and $\psi(\cdot)$ as a perturbation using the first-order Taylor approximation resulting in

$$\begin{aligned}
\mathsf{n}_1 &\approx \mathbf{m}_{\mathrm{t}}^{\mathrm{T}} \left(\frac{\partial \tau(\boldsymbol{u}, \boldsymbol{p}_{\mathrm{t}}, \boldsymbol{p}_{\mathrm{r}})}{\partial \boldsymbol{p}_{\mathrm{t}}} \right) + \mathbf{m}_{\mathrm{r}}^{\mathrm{T}} \left(\frac{\partial \tau(\boldsymbol{u}, \boldsymbol{p}_{\mathrm{t}}, \boldsymbol{p}_{\mathrm{r}})}{\partial \boldsymbol{p}_{\mathrm{r}}} \right) + \mathsf{m}_{\mathrm{RTT}} \\
\mathsf{n}_2 &\approx \mathbf{m}_{\mathrm{a}}^{\mathrm{T}} \left(\frac{\partial \theta(\boldsymbol{u}, \boldsymbol{p}_{\mathrm{a}})}{\partial \boldsymbol{p}_{\mathrm{a}}} \right) + \mathsf{m}_{\mathrm{az}} + \mathsf{m}_{\mathrm{AOA,az}} \\
\mathsf{n}_3 &\approx \mathbf{m}_{\mathrm{a}}^{\mathrm{T}} \left(\frac{\partial \psi(\boldsymbol{u}, \boldsymbol{p}_{\mathrm{a}})}{\partial \boldsymbol{p}_{\mathrm{a}}} \right) + \mathsf{m}_{\mathrm{on}} + \mathsf{m}_{\mathrm{AOA,on}} \,.
\end{aligned}$$

Ultimately, this Taylor approximation simplifies to a weighted sum of independent scalar Gaussian noise distributions. Although there is a slight dependence on $\boldsymbol{u}$ and the other parameters in the model, this was verified to be negligible via simulation. We placed UEs at various locations distributed throughout the satellite FoV and verified a negligible change in the approximated noise model. The resulting random noise vector can clearly be approximated using a single multivariate Gaussian PDF.

B. LVS Performance Evaluation

We evaluated the performance of the presented noise model approximation by generating a true user position and noisy measurement vector $\tilde{\boldsymbol{\eta}}$ as detailed in (8a)-(8c). For each measurement, we simulated a compliant UE which reported its true location, and a malicious UE which reported a random position outside the acceptance region. Repeating the process outlined in Algorithm 2 many times, we estimated the Type I (false alarm) and Type II (missed detection) error probabilities for various threshold values using each decision rule. The overall ROC curves for the three decision rules are shown in Fig. 2, varying $\chi \in [0, \infty)$. We compare the performance of the proposed method $R(\boldsymbol{\eta}; \mathcal{A})$, as described in (14), with both baseline strategies $B_1(\boldsymbol{\eta}; \boldsymbol{u}_{\mathrm{c}})$ and $B_2(\boldsymbol{\eta}; \mathcal{A})$, as described in (15)-(16).

As the likelihood function and acceptance region change based on the malicious UE's reported location, we evaluated the performance of the LVS at different "spoofing distances" $\|\boldsymbol{u}_{\mathrm{c}} - \boldsymbol{u}\|$. Fig. 3 shows the LVS performance at close spoofing distances (between 5 km and 15 km) and far spoofing distances (between 15 km and 25 km). Finally, Fig. 4 compares the area under the ROC curve (AUC) for each decision rule when the spoofing distance is 5-15 km, 15-25 km, or randomly chosen. The AUC provides a generalized performance metric ranging between 0 and 1 for a decision system over all thresholds, and it is calculated by integrating the ROC curve. Note that the LVS consistently detected any malicious users beyond 25 km from their reported positions, so the ROC curve for distances greater than 25 km is trivial. The most significant improvement in AUC is observed at close spoofing distances between 5-15 km. As shown in Fig. 4, the proposed LVS outperforms the GLRT decision rule by 19.3% and the reported likelihood decision rule by 35.4%. On average, the proposed integrated likelihood ratio decision rule outperforms the GLRT AUC by 9.6% and the reported likelihood AUC by 12.0%.

V. Conclusion

This paper proposes a reliable likelihood-based LVS for NTNs in xG networks. The system fuses RTT and AOA measurements from a single satellite into an integrated likelihood ratio decision rule. We consider several uncertainty sources in the NTN scenario and approximate their effects with a GMM. We implemented a hypothesis test for detecting spoofed location information by exploiting AOA and RTT information. Through simulation, we analyzed the performance of the LVS using the derived noise model when the true error followed the more general noise model. For the input error distribution assumed in this paper, choosing the GMM with the

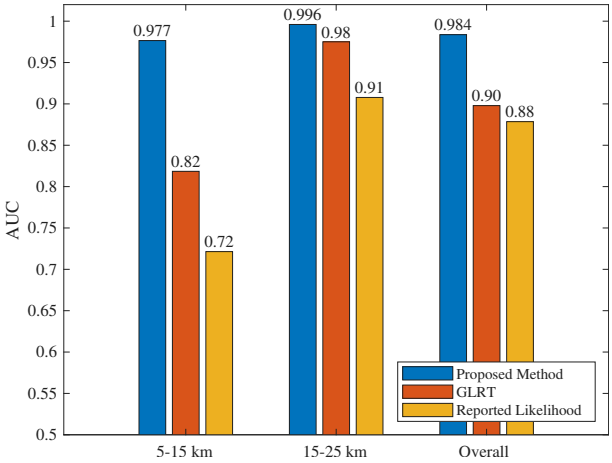

Fig. 4: AUC performance of the proposed LVS at different spoofing distances. The proposed integrated likelihood ratio strategy is compared against two baseline decision rules, as displayed in Figs. 2 and 3.

minimum AIC consistently resulted in a single Gaussian noise distribution. This noise model was able to consistently discriminate between legitimate and malicious UEs. However, the framework can be easily extended to an arbitrary uncertainty distribution and acceptance region geometry using empirical data. For many input distributions, a GMM can accurately describe the scenario of a given satellite constellation without significantly increasing the complexity of the overall model. By enabling NTN network verified location, this LVS can help ensure the security of global cellular coverage using LEO constellations.

REFERENCES

[1] M. Z. Win, A. Conti, S. Mazuelas, Y. Shen, W. M. Gifford, D. Dardari, and M. Chiani, "Network localization and navigation via cooperation," *IEEE Commun. Mag.*, vol. 49, no. 5, pp. 56–62, May 2011.

[2] *Technical Specification Group Services and System Aspects; Functional stage 2 description of LCS (Release 18)*, 3rd Generation Partnership Project 3GPP™ TS 23.271 V18.0.0, Mar. 2024, release 18.

[3] M. Z. Win, Y. Shen, and W. Dai, "A theoretical foundation of network localization and navigation," *Proc. IEEE*, vol. 106, no. 7, pp. 1136–1165, Jul. 2018, special issue on *Foundations and Trends in Localization Technologies*.

[4] A. Conti, F. Morselli, Z. Liu, S. Bartoletti, S. Mazuelas, W. C. Lindsey, and M. Z. Win, "Location awareness in beyond 5G networks," *IEEE Commun. Mag.*, vol. 59, no. 11, pp. 22–27, Dec. 2021.

[5] A. Vanelli-Coralli, A. Guidotti, T. Foggi, G. Colavolpe, and G. Montorsi, "5G and Beyond 5G Non-Terrestrial Networks: trends and research challenges," in *Proc. IEEE 3rd 5G World Forum (5GWF)*, Oct. 2020, pp. 163–169.

[6] G. Kwon, W. Shin, A. Conti, W. C. Lindsey, and M. Z. Win, "Access-backhaul strategy via gNB cooperation for integrated terrestrial-satellite networks," *J. Sel. Areas Commun.*, vol. 42, no. 5, pp. 1403–1419, May 2024.

[7] F. Rinaldi, H.-L. Maattanen, J. Torsner, S. Pizzi, S. Andreev, A. Iera, Y. Koucheryavy, and G. Araniti, "Non-terrestrial networks in 5G & beyond: A survey," *IEEE Access*, vol. 8, pp. 165 178–165 200, 2020.

[8] H. Dureppagari, C. Saha, H. Dhillon, and M. Buehrer, "NTN-Based 6G Localization: Vision, Role of LEOs, and Open Problems," *IEEE Wireless Commun.*, vol. 30, no. 6, pp. 44–51, 2023.

[9] *Technical Specification Group Radio Access Network; Study on requirements and use cases for network verified UE location for NTN in NR (Release 18)*, 3rd Generation Partnership Project 3GPP™ TR 38.882 V18.0.0, Jun. 2022, release 18.

[10] A. Conti, S. Mazuelas, S. Bartoletti, W. C. Lindsey, and M. Z. Win, "Soft information for localization-of-things," *Proc. IEEE*, vol. 107, no. 11, pp. 2240–2264, Nov. 2019.

[11] F. Morselli, S. M. Razavi, M. Z. Win, and A. Conti, "Soft information-based localization for 5G networks and beyond," *IEEE Trans. Wireless Commun.*, vol. 22, no. 12, pp. 9923–9938, Dec. 2023.

[12] S. Cakaj, B. Kamo, A. Lala, and A. Rakipi, "The coverage analysis for low earth orbiting satellites at low elevation," *Int. J. Adv. Comput. Sci. and Appl.*, vol. 5, no. 6, pp. 6–10, 2014.

[13] M. Ozger, I. Godor, A. Nordlow, T. Heyn, S. Pandi, I. Peterson, A. Viseras, J. Holis, C. Raffelsberger, A. Kercek *et al.*, "6G for connected sky: A vision for integrating terrestrial and non-terrestrial networks," in *Proc. Joint Eur. Conf. Netw. Commun. 6G Summit (EuCNC/6G Summit)*, 2023, pp. 711–716.

[14] N. S. Kanuri, S.-Y. Chang, Y. Park, J. Kim, and J. Kim, "Impact of location spoofing attacks on performance prediction in mobile networks," in *Silicon Valley Cybersecurity Conf.* Springer Nature Switzerland Cham., 2022, pp. 107–119.

[15] J. Wigard, E. Juan, J. Stanczak, M. Lauridsen, A. Marcone, S. Hoppe, A. Ahmadzadeh, A. Masri, and D. H. Tran, "Ubiquitous 6G service through non-terrestrial networks," *IEEE Wireless Commun.*, vol. 30, no. 6, pp. 12–18, Dec. 2023.

[16] S. Li, Q. Zhang, B. Deng, B. Wu, and Y. Gao, "A fast and accurate LEO satellite-based direct position determination assisted by TDOA measurements," *China Commun.*, vol. 19, no. 1, pp. 92–103, Jan. 2022.

[17] G. Laveti, G. S. Rao, D. E. Chaitanya, and M. Kumar, "TDOA measurement based GDOP analysis for radio source localization," *Procedia Comput. Sci.*, vol. 85, pp. 740–747, 2016.

[18] S. Nawaz, E. Cianca, T. Rossi, and M. De Sanctis, "Round Trip Time (RTT) and Doppler Measurements for IoRT Localization by a Single-Satellite," *IEEE Commun. Lett.*, Dec. 2023.

[19] X. Lin, Z. Lin, S. E. Lowenmark, J. Rune, R. Karlsson *et al.*, "Doppler shift estimation in 5G new radio non-terrestrial networks," in *Proc. IEEE Global Commun. Conf. (GLOBECOM)*, Dec. 2021, pp. 1–6.

[20] M. El Jaafari, N. Chuberre, S. Anjuere, and L. Combelles, "Introduction to the 3GPP-defined NTN standard: A comprehensive view on the 3GPP work on NTN," *Int. Satell. Commun. Netw.*, vol. 41, no. 3, pp. 220–238, Feb. 2023.

[21] G. Cai, B. M. Chen, T. H. Lee, G. Cai, B. M. Chen, and T. H. Lee, *Unmanned Rotorcraft Systems*. London: Springer-Verlag, 2011.

[22] J. Clynch, "Geodetic Coordinate Conversions," *Geodetic to/from Geocentric Latitude*, 2006.

[23] S. Casotto, "The equations of relative motion in the orbital reference frame," *Celestial Mechanics and Dynamical Astronomy*, vol. 124, no. 3, pp. 215–234, Nov. 2016.

[24] P. Paalanen, J.-K. Kamarainen, J. Ilonen, and H. Kalviainen, "Feature representation and discrimination based on gaussian mixture model probability densities—Practices and algorithms," *Pattern Recognition*, vol. 39, no. 7, pp. 1346–1358, Jul. 2006.

[25] T. Ma and A. Ng, "CS229 Lecture notes: The EM algorithm," Lecture Notes, 2019.

[26] J. Neyman and E. Pearson, "On the problem of the most efficient tests of statistical hypotheses," *Phil. Trans. Roy. Soc. London A, Math. Phys. Sci.*, vol. 231, no. 694-706, pp. 289–337, Feb. 1933.

[27] O. Zeitouni, J. Ziv, and N. Merhav, "When is the generalized likelihood ratio test optimal?" *IEEE Trans. Inform. Theory*, vol. 38, no. 5, pp. 1597–1602, Sep. 1992.

[28] B. Bissinger, "AST SpaceMobile Deploys Largest-Ever Commercial Communications Array in Low Earth Orbit," *Business Wire*, 2022.

[29] X. He, U. Hugentobler, A. Schlicht, Y. Nie, and B. Duan, "Precise orbit determination for a large LEO constellation with inter-satellite links and the measurements from different ground networks: a simulation study," *Satell. Navigat.*, vol. 3, no. 1, p. 22, Oct. 2022.

[30] D. Brasoveanu, J. Hashmall, and D. Baker, "Spacecraft attitude determination accuracy from mission experience," in *NASA Conf. Pub.* NASA, 1994, p. 153.

[31] A. Bahillo, S. Mazuelas, R. Lorenzo, P. Fernandez, J. Prieto, R. Duran, and E. Abril, "Hybrid RSS-RTT localization scheme for indoor wireless networks," *EURASIP J. Adv. Signal Process.*, vol. 2010, no. 1, pp. 1–12, Mar. 2010.

[32] W. Xu, M. Huang, C. Zhu, and A. Dammann, "Maximum likelihood TOA and OTDOA estimation with first arriving path detection for 3GPP LTE system," *Trans. Emerg. Telecommun. Technol.*, vol. 27, no. 3, pp. 339–356, Mar. 2016.

[33] T. Filik and T. E. Tuncer, "Uniform and nonuniform V-shaped planar arrays for 2-D direction-of-arrival estimation," *Radio Sci.*, vol. 44, no. 05, pp. 1–12, Oct. 2009.